THESIS FOR THE DEGREE OF LICENTIATE OF ENGINEERING IN SOLID AND STRUCTURAL MECHANICS

X-ray computer tomography based numerical modelling of fibre reinforced composites

ROBERT MICHAEL AUENHAMMER

Department of Industrial and Materials Science
Division of Material and Computational Mechanics
CHALMERS UNIVERSITY OF TECHNOLOGY

Göteborg, Sweden 2021

X-ray computer tomography based numerical modelling of fibre reinforced composites
ROBERT MICHAEL AUENHAMMER

Thesis for the degree of Licentiate of Engineering IMS-2021-9
ISSN 1652-8565
Department of Industrial and Materials Science
Division of Material and Computational Mechanics
Chalmers University of Technology
SE-412 96 Göteborg
Sweden
Telephone: +46 (0)31-772 1000

Cover:
Result of a finite element model solely based on X-ray computer tomography data of a non-crimp reinforced polymer

Chalmers Reproservice
Göteborg, Sweden 2021

X-ray computer tomography based numerical modelling of fibre reinforced composites

ROBERT MICHAEL AUENHAMMER
Department of Industrial and Materials Science
Division of Material and Computational Mechanics
Chalmers University of Technology

Abstract

Non-crimp fabric reinforced polymers are commonly used to manufacture the load carrying parts in wind turbine blades. Since wind turbine blades have a large material usage, the favourable stiffness to price ratio of non-crimp fabric reinforced polymers is highly attractive for manufactures. Additionally, they are easy to manufacture, which is essential for mould sizes of up to approximately 100 m. Smaller turbine blades up to 75 m use glass fibres, lager blades require carbon fibres to meet the stiffness requirements.
Wind turbine blades are ever increasing in length since the generated power is proportional to the length squared. In addition to the challenge to reduce the material usage, longer blades demand higher stiffness. Furthermore, wind turbines are one of the man-made structures that have to endure the highest numbers of load cycles. Even though wind turbine blades are mainly loaded in tension there are compressive loads present on the leeward side of the blade. Those three main material requirements demand highly tailored high-performance materials. At the same time wind turbine manufactures are under a high cost pressure as governments all over the world are cutting subsidies. As for any other high-performance material a constant production quality is essential. Yet, in particular composites are susceptible for manufacture flaws.
X-ray computer tomography allows for the detection of some of the defects present after manufacture. X-ray computer tomography is a very promising tool for materials quality control and quantification when combined with numerical modelling. In the last years the image acquisition and analysis process has seen enormous progress that can now be exploited.
In this research project the X-ray computer tomography aided engineering (XAE) process has been established. XAE systemically combines all work-steps from material image acquisition to the final finite element analysis results. The process provides an automated, accurate and fast image analysis and an element-wise and integration point-wise material orientation mapping. The analysis of the detailed stress and strain distributions after manufacture with XAE will allow for more reliable and low-cost wind turbine blades.

Keywords: Composites, X-ray computer tomography, Segmentation, Finite element modelling

Avancez

Preface

Before I joined the Mummering (MUltiscale, Multimodal and Multidimensional imaging for EngineeRING) project (Grant number 765604) I did not know much about tomography. However, working for over two years in this field has convinced me of the huge possibilities tomography has to offer.

Acknowledgements

I would like to express my sincere gratitude to the organisers of this Intensive Training Network. Our workshops and events not only convey at lot of knowledge in tomography and its applications but also enable many collaborations and friendships among us fifteen Early Stage Researchers.

At this point I would also like to thank the European Commission and especially the European tax payers that enable us participating in and obtaining this extraordinary education and for the financial support of our research.

Moving to a new country, learning a new language and being a PhD student can be challenging but all my colleagues and friends at Chalmers were very supportive and made life much easier for me. I am very grateful for that.

I would like to give a special thanks to my former supervisor Brina Blinzler who sadly left Chalmers. I am glad that Ragnar Larsson stepped in as a replacement and became an active member in our project.
Without my supervisor Lars Mikkelsen from DTU this project would never have been possible in the first place. And without his expertise in computer tomography, composites and modelling I would have had a much tougher time during my first two years. Thank you very much!
I am especially grateful for my main supervisor Leif Asp who convinced me to take this position and for his excellence guidance as well as support for my ideas. Moreover, he was very patient talking only Swedish with me after a couple of months at a time where I could hardly speak Swedish.

I am really happy that my old friendships lasted over distance and especially during times where travels are restricted. I am very grateful for every phone call.

Finally, heartfelt thanks go my family for their love and support at all times.

Thesis

This thesis consists of an extended summary and the following appended papers:

Paper A R. M. Auenhammer, L. P. Mikkelsen, L. E. Asp, B. J. Blinzler. Automated X-ray computer tomography segmentation method for finite element analysis of non-crimp fabric reinforced composites. Composite Structures 256 (2021), 113136. DOI: 10.1016/j.compstruct.2020.113136.

Paper B R. M. Auenhammer, N. Jeppesen, L. P. Mikkelsen, V. A. Dahl, B. J. Blinzler, L. E. Asp. X-ray computer tomography aided engineering for non-crimp fabric reinforced composites. To be submitted.

Other peer-review publications related to thesis but not attached

Publication I R. M. Auenhammer, L. P. Mikkelsen, L. E. Asp, B. J. Blinzler. X-ray tomography based numerical analysis of stress concentrations in non-crimp fabric reinforced composites - assessment of segmentation methods. IOP Conference Series: Materials Science and Engineering 942 (2020), 012038. DOI: 10.1088/1757-899X/942/1/012038.

Publication II R. M. Auenhammer, L. P. Mikkelsen, L. E. Asp, B. J. Blinzler. Dataset of non-crimp fabric reinforced composites for an X-ray computer tomography aided engineering process. Data in Brief 33 (2020), 106518. DOI: 10.1016/j.dib.2020.106518.

Contents

Part I
Extended Summary

1 Introduction

Despite discussions on CO_2 emissions extending over decades and the *Kyoto Protocol* signed in 1997, global CO_2 emissions reached a new maximum in 2018 [1]. Similar to the *Millennium Development Goals* new goals for 2030 were agreed on in the United Nations General Assembly on the 25^{th} of September 2015 [2]. They are called the *Sustainable Development Goals*. Beside ending all forms of poverty and fighting inequalities, tackling global climate change is a key goal. On December 17^{th} 2019 the European Commission presented the *European Green Deal* supported by a one trillion Euro fund which should lead to a *European Climate Law* [3]. The objective is zero net emission of greenhouse gases until 2050, and at the same time decoupling economical growth from resources usage. These ambitious goals require many simultaneous actions that need to be implemented quickly.

Wind turbines will be one of the key technologies for the transition from fossil fuel based energy to renewable energy [4]. They come with the advantage of a drastic reduction in CO_2 emissions as well as the possibility to reduce inequalities between countries. At the moment a select few countries are exporting oil and gas needed by the rest of the world. This leads directly to the problems of corruption and cartels [5]. In the future all countries will be able to install wind turbines to secure their own independent energy source.

This research project aims to contribute to the increased attractiveness of wind power by reducing development and material costs of wind turbines.

1.1 Wind power potential

Globally in 2019, an offshore wind power supply of only 23 GW was available, corresponding to 0.8 % of the global electrical power generation. Approximately 80 % of this was installed in Europe [1]. However, the growth possibilities are enormous. Notably an annual production potential of 36 000 TWh in Europe in regions close to shores with shallow waters is identified [1]. New floating turbines in deeper waters could multiply this number. In comparison to the offshore production potential a yearly global electrical energy of 23 000 TWh is currently generated.

In Figure 1.1 it can be seen, that the European Union in particular has a huge potential for offshore wind energy production. The two world market leaders in wind turbine manufacture *Siemens Gamesa Renewable Energy S.A.* and *MHI Vestas Offshore Wind A/S* are both European companies. In 2018 they accounted for 71 % of a multi billion euro market [1]. The entire wind industry is determined to ramp up the installed wind energy power to 2 TW and triple the jobs to four million by 2030 [7]. This requires a significant production capacity enhancement. The scaling effects will lead to a further

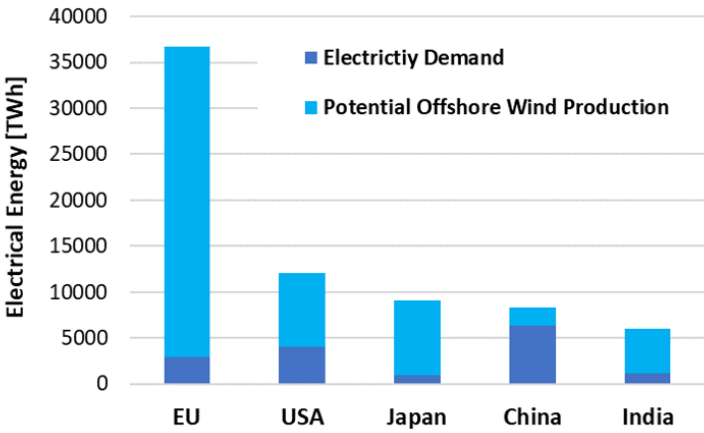

Figure 1.1: *Annual electrical energy demand and potential for offshore wind energy production in selected countries in 2018. EU is including the United Kingdom in this figure. [6]*

price reduction. At auctions for offshore power plants in Europe with current prices of approximately 50 €/MWh some projects do not require any subsidies at all [1]. That means they will be able to compete with other electrical energy sources when production begins in a couple of years. These competitive prices however include a bet on future development improvements leading to cost reductions.

1.2 Wind turbine blades

The offshore wind turbine cost (CoTu) accounts for approximately 40 % of the total upfront cost to be able to supply electrical energy to the grid [1]. The other main upfront costs are installation (CoI), foundation (CoF) and transmission (CoTr). To those upfront costs the maintenance costs (CoM) and the cost of recycling (CoR) are added which leads to the definition of the cost of energy (CoE) in Equation 1.1 with $P_{turbine}$ as turbine power.

$$CoE = \frac{CoTu + CoI + CoF + CoTr + CoM + CoR}{P_{turbine}} \tag{1.1}$$

Regarding wind turbine blades, two main measures have an impact on the energy cost reduction. One is to improve the fatigue behaviour of the blades in order to reduce the maintenance cost. For this purpose the fatigue process needs to be better understood. The other measure is to increase the wind turbine power while keeping the cost of the turbine low. From the generated wind power in Equation 1.2, where A is the swiped area, v the wind speed and C_p the power coefficient, it becomes clear how this can be achieved. The swiped area A is directly proportional to the blade length squared and so

is the generated power.

$$P_{turbine} = \frac{1}{2}\rho A v^3 C_p \tag{1.2}$$

This is the reason why the wind turbines are constantly increasing in size. Figure 1.2 shows the development of the offshore wind turbine sizes over the last ten years with a prediction for 2030 compared with the height of the Eiffel Tower.

Longer blades require a higher stiffness due to the higher aerodynamic and gravitational loads. At the same time the mass and cost need to remain low. This challenge can be only solved with fibre reinforced composites. For shorter blades glass fibres are sufficient, however longer blades will require carbon fibres, even though they are more expensive. Wind turbine blades are among the man-made structures that have to endure the most

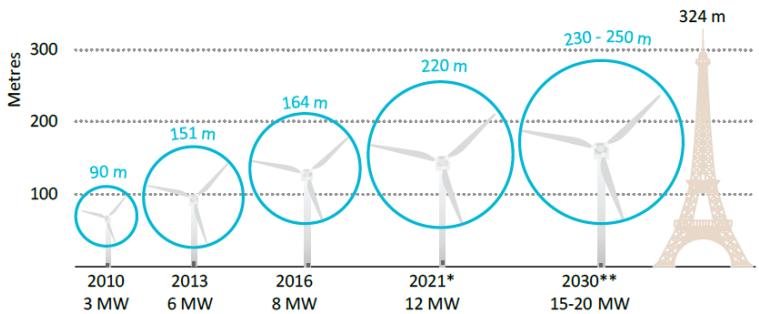

Figure 1.2: *Largest commercially available wind turbines since 2010 and a prediction for 2030. (Printed with permission from the International Energy Agency [6].)*

load cycles. Over a lifetime of approximately 25 years 50 to 300 million cycles are experienced by a blade [8]. This is much more than cars or aeroplanes are exposed to. In addition to the extreme fatigue and the stiffness requirements a high compressive strength is necessary due to the pressure stresses on the leeward side of the blade.
These key material parameters cannot only be developed further by using more advanced materials but also by improving the structure itself on all scales from the single fibre over the composite lay-up to the whole blade design.

1.3 Objective

To achieve the green transition goals of the United Nations and the European Commission wind energy needs to play a key role and exploit its potential. Central for a successful development are cheap and long lasting wind turbines. This project can contribute to this goal by improving the structure of wind turbine blades on the fibre and fibre to matrix interface scale. In particular the tensile stiffness, the fatigue behaviour and the compressive strength are of interest. A methodology is developed to utilise the recent progress in X-ray computer tomography and combine it with finite element modelling. With this novel approach the development of improved composites for wind turbine blades shall be cheaper and faster.

2 Research scope

This is one of the first projects that systematically combines X-ray computer tomography with finite element modelling on multiple scales for fibre reinforced composites. In the following the different project aspects are described in more detail.

2.1 Non-crimp fabric reinforced composites

Non-crimp fabrics embedded in a polymer matrix are commonly used as fibre lay-up in wind turbine blades. As manufacture methods liquid moulding technologies like resin transfer moulding or vacuum infusion are common. They are regarded as comparatively cheap [9]. Originally developed for aeronautic structural parts [10] non-crimp fabrics reinforced composites are nowadays used in many other applications e.g. automotive and wind industry [11].

One of their main advantages beside the ease of manufacture is their high in-plane stiffness to weight ratio. The out-of-plane properties on the other hand are rather poor. Thus, they are tailored to take loads mostly in in-plane direction. Figure 2.1 visualises the reason therefore. It shows an exemplary layup with mainly unidirectional bundles that are held together by backing bundles and stitching threads. This structure is characterised by areas with a high local volume fraction inside the unidirectional bundles. The distribution of fibres inside the bundle is usually even, although manufacture issues can cause local resin pockets and twisted fibres. Outside the unidirectional bundles resin rich areas are the consequence for this layup. However, the major effect on the material properties is caused by the waviness of the unidirectional bundles. The in-plane waviness is induced by the backing bundles and the stitching threads while the out-of-plane waviness comes from the compaction in the production process [12]. The material parameters of a non-crimp

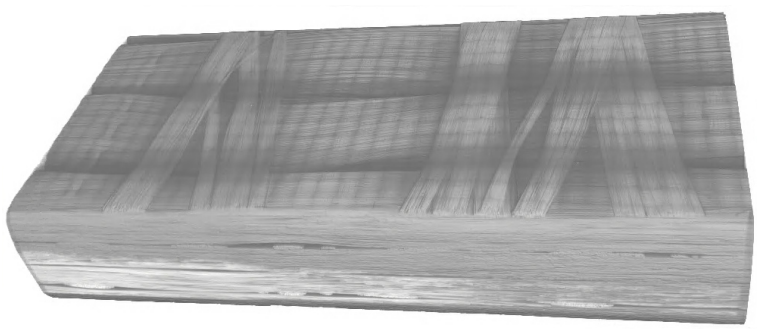

Figure 2.1: *Visualisation of the architecture of a non-crimp fabric glass fibre reinforced composite with a rendered X-ray computer tomography image.*

fabrics reinforced composite are determined consequently by many factors. On the fibre scale, the fibre orientation is mostly effected by the bundle waviness but also by a local more independent fibre orientation, e.g. twisting. Those fibre misalignments influence

the stiffness of the entire composite. The compression strength though is affected even more severely by the fibre misalignment [13], [14]. In addition, it has been shown that the fatigue process starts on the fibre scale [15], [16]. The matrix to bundle interface is important for the fatigue progress, e.g. how the crack growth can be stopped. On the fibre bundle level the waviness of the bundles with all its described consequences, the stacking sequence and the global fibre volume fractions which are decisive for the global stiffness properties are governing. These properties characterise non-crimp fabrics reinforced composite as a heterogeneous material.

Modelling this heterogeneous material behaviour becomes challenging. Models that intend to simulate the elastic stiffness properties are relatively easy and accurate [17], [18]. Modelling strength and fracture is considerably more difficult. The different phenomena on all levels need to be included to create an accurate model. This is particularly unpractical for large structures. To make the models more accessible it is often focused on the governing failure mode(s). The geometry feature with the largest influence on the mechanical properties is the bundle waviness [19]. The bundle waviness is rather irregular. It changes from bundle to bundle and differs even within a bundle [20]. However, many models for non-crimp reinforced composite approximate the waviness with sine functions [21], [22]. The fibre orientation follows thereby the orientation of the bundle. Local orientations are hence not included. In recent years many studies aimed to model different failure modes e.g. a compressive failure analysis [23], a study about combined compression and shear loading [24], an investigation of transverse tensile and transverse compressive strength [25], a damage mechanisms analysis under static and fatigue loading [26], a compressive loading study [27] and a fibre kinking analysis [28].

Those models are mostly excluding manufacture deviation and defects. Models based on X-ray computer tomography can respect those effects. As mentioned earlier some phenomena are induced by the manufacture process and hence can only be detected in the real part. X-ray computer tomography based models are comparatively complicated since they introduce the step of the image analysis, so called segmentation. Despite their increased complexity and time intensity computer, tomography image data based models will become more common due to their ability to reflect manufacture deviations and capture non-destructively time-dependent material behaviour.

2.2 X-ray computer tomography

X-ray computer tomography has emerged from its initial application field in medical diagnosis in the 1960s to non-medical research and industrial purposes in the following decades [29]. The demand for 3D imaging in various fields has triggered active research in computer tomography. In particular developments in image acquisition as well as the follow-up processes reconstruction and segmentation made the technology broadly applicable with affordable computer tomographic scanners for medical as well as industrial and academic utilisation.

It bases on common radiography, discovered by Wilhelm Röntgen in 1895, with the physical principle that an X-ray beam is attenuated on its propagation through a material due to scattering and absorption. It follows the Beer-Lambert's law (Equation 2.1) where

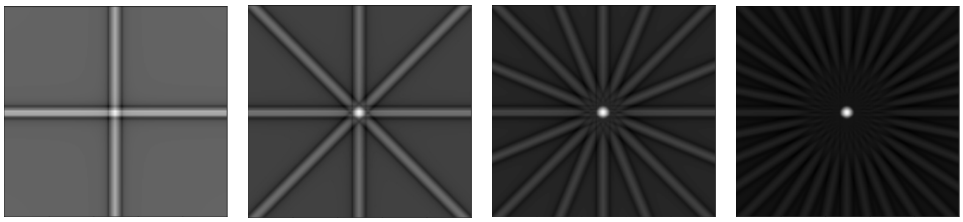

(a) *2 projections* (b) *4 projections* (c) *8 projections* (d) *16 projections*

Figure 2.2: *Reconstruction of a point with the method Filtered Backprojection with 2, 4, 8 and 16 projections with the ASTRA Tomography Toolbox [42]. More projections would further increase the quality of the reconstruction.*

I represents the recorded x-ray intensity, I_0 the initial x-ray intensity, x the part of propagated X-rays and μ the linear attenuation coefficient of the material [30].

$$I = I_0 e^{-\mu x} \tag{2.1}$$

The linear attenuation coefficient μ (Equation 2.2) itself depends on the density of the material ρ, the atomic number Z, the initial energy of the X-ray photons E and a constant K.

$$\mu = K\rho\frac{Z}{E} \tag{2.2}$$

This leads to different contrasts for different materials in the 2D projections on the detector which consists of a photosensitive material divided into a finite number of pixels. Due to a rotation of either the object or the detector and source a 3D information about size and position can be added. Consequently, a tomography scan is built of a finite number of 2D projections. The 2D projections combined deliver a collection of line integrals [31].

With reconstruction a 3D image is shaped from the line integrals. This inverse problem can be solved analytically or iteratively [32]. The most common analytical method is the *Filtered Backprojection* (Figure 2.2). Back-projection describes the smearing of the projection in every single detector pixel back in the direction of the X-ray beam. The filtering of the projections before the back-projections results in better reconstructions [33]. With an infinite number of projections the real dimension and position of the scanned object(s) can be reconstructed [34]. Despite the very fast computation times of *Filtered Back-Projection*, it has limitations in accuracy stemming from limited numbers of projections [35]. Additionally, physical effects like beam-hardening can cause severe issues during reconstruction [36].

Iterative algorithms offer alternative solutions. They can be distinguished in algebraic [37] and statistical [38]. They treat the reconstruction process as a system of linear equations and can be adapted for various challenges. The progress in *Deep Learning* and computational power gave rise to many new applications [39], [40], [41]. A constant challenge for all reconstruction algorithms lies in the suppression of artefacts [43]. In reconstruction all inaccurate details and objects in the reconstructed images are called artefacts (Figure 2.3), i.e. incorrect vertical elongation and disappearance of horizontal

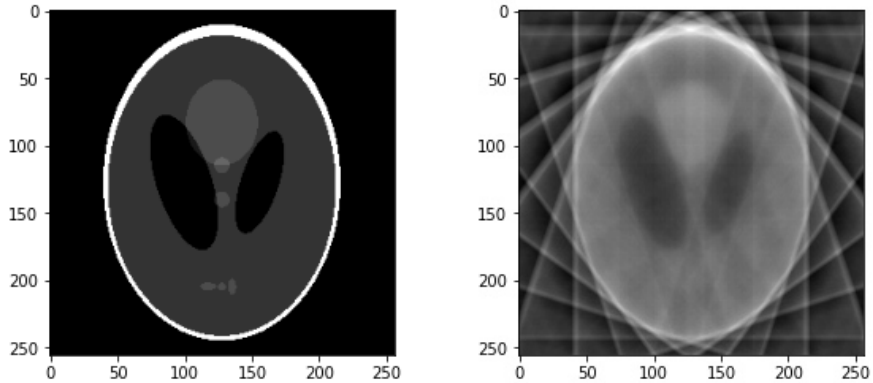

Figure 2.3: *Reconstructed image with artefacts (right) of a phantom image (left) created with the ASTRA Tomography Toolbox [42].*

structures. They can originate from high cone-angles [44] or real-time reconstruction algorithms for synchrotron applications [45].

Traditional material characterisation based on imaging such as microscopy requires a destruction of the sample. This downside created the demand for non-destructive imaging technologies. X-ray computer tomography offers supreme options for characterising important material parameter for complex micro-structures [46]. This non-destructive 3D imaging technique combines multi-scale, multi-modal, time-lapse options that add vast characterisation options. It is not only applied for composites but also for metals or concrete materials [47], [48], [49].

X-ray computer tomography scans of composites can be performed to evaluate manufacture processes, tensile failure, compressive failure and kinking, fatigue as well as impact damage [50]. Although X-ray computer tomography offers lower resolutions than scanning electron microscopes, single fibres can be easily resolved and tracked [51]. Material behaviour correlation with tomography scanners can be performed *in-situ* and *ex-situ*. For the *in-situ* method the scanned sample is exposed to a load during scanning, while for the *ex-situ* method the sample is first applied with a load and then scanned. The *in-situ* method is beneficial since the mounting and focusing process of the sample must be only carried out once. Additionally, the material behaviour under loading can be studied. However, more common is the *ex-situ* technique, due to various reasons such as the limited space for material testing inside a scanner and long scanning times (range of several hours for lab-based scanners). Compressive failure tests with abrupt fibre kinking [52] are very difficult to capture and hence usually performed *ex-situ*. Nevertheless, Wang et al. [53] could report an *in-situ* four-point-bending test. Furthermore, the latest research has pushed the limits and opens new possibilities for *in-situ* approaches with self-learning [54] and real-time reconstruction [55] algorithms.

2.3 Segmentation

Segmentation describes the analysis of X-ray computer tomography images. Without efficient segmentation algorithms terabytes of generated image data remain unused. Only segmentation allows for quantitative assessments of the images. Yet, segmentation algorithms for complex quantifications must be frequently tailored for individual samples. They are often complex to design and require extensive computational efforts. The segmentation options are partly determined by the acquisition parameters and the desired modelling goal. Hence, already before the image acquisitions a clear goal for the segmentation and modelling should be defined. The desired region of interest and fibre resolution determines the voxel size for scanning. The required grey-scale contrast for proper segmentation defines the scanning technology.

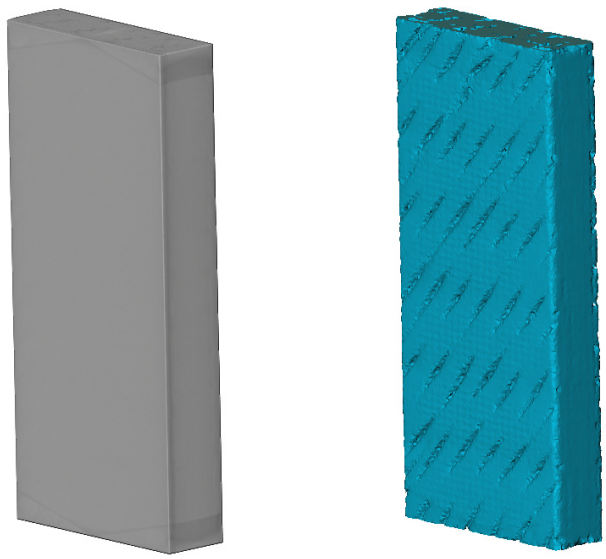

(a) *Original computer tomography image*

(b) *Fibre bundles surface after thresholding*

Figure 2.4: *Thresholding can remove the resin-rich areas from the original image (a) due to the higher grey-scale value of the resin. With the surface generation in Avizo™ [56] a geometry of the fibre bundles can be generated (b). On the top and bottom of the original image (a) a triangular shape is visible. This originates from cone beam effects from the image acquisition.*

The simplest segmentation method is called thresholding where two or more different materials can be separated due to their different grey-scale value in the scanned image. Since the matrix has a higher grey-scale value than the glass fibres they can be segmented easily. For carbon fibres it becomes more difficult as their grey-scale value is in the same

Figure 2.5: *Vector visualisation that represent the tracked fibres of a non-crimp fabric reinforced composite in Avizo™. The main fibre orientation is out of plane, the horizontal lines represent fibres in the backing bundles.*

range as for the matrix. Figure 2.4 depicts an original image of a scanned non-crimp reinforced composite and the thresholded boundary surface between the resin-rich areas and the fibre bundles. This surface is represented with a mesh of triangular elements. There are thresholding operators in nearly all segmentation software packages as well as Matlab and Python functions.

For composite modelling usually a material orientation and some form of boundary representation between fibre and matrix or between fibre bundles and matrix is necessary. The options for material orientation segmentation are manifold. One method is a global fibre orientation following the bundle waviness [57]. In contrast to the above described sine function approximations, single bundles must be segmented to create a centre line that represents the bundle waviness. For larger structures this can be a legitimate approach. It limits though the degree of detail of local fibre orientations that can be modelled later on.

Another option is individual fibre tracking (Figure 2.5). There a commercial possibilities like Avizo™ *XFiber* [56] from Thermo Fisher Scientific or solutions based on a machine learning approach [58], ellipsometry [59], [60] or particle tracking [61]. Those codes supply comprehensive information about fibre orientation and position, but require high resolution images and computational effort. Further, substantial user interaction is necessary. In larger structures with hundreds of thousand fibres often the single fibre orientation is less important than an accurate mean fibre orientation estimation [62],[63].

Structure tensor methods can overcome these obstacles. In the studies of Tucker with Advani [64] and Bay [65] the foundation for modern structure tensor codes was laid. It was originally developed to predict the fibre orientation of injection moulded short fibre composites. Later it was adapted to capture the material orientation of composites [66], [67].

A structure tensor[1] in 3D image analysis is defined by a 3×3 matrix which represents the material orientation in the neighbourhood around a point within the regarded volume [70]. With $\nabla V = [V_x \; V_y \; V_z]^T$ as gradient of the volume V the structure tensor is computed

[1]Those structure tensors should not be confused with structural tensor approaches in mechanics as for example in [68] or [69]

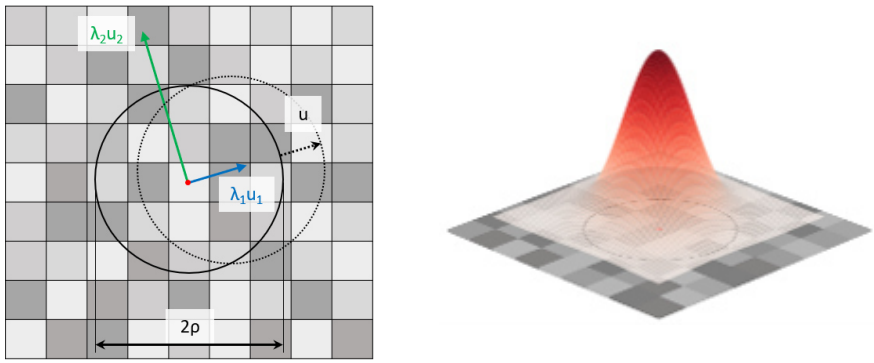

Figure 2.6: *Form of visualisation of the structure tensor analysis method in two dimensions. The pixel with the red dot represents the currently regarded pixel. The black circle with the radius ρ reflects the standard deviation of the Gaussian kernel K_ρ. The structure tensor calculates the sum of squared differences of grey-scale values in a certain direction (exemplary visualised with dashed circle). The two orthogonal eigenvectors of the structure tensor u_1 and u_2 are multiplied with the corresponding eigenvalues λ_1 and λ_2. The smallest eigenvalue defines the predominant material orientation.*

with Equation 2.3.

$$S = \sum \nabla V (\nabla V)^T \tag{2.3}$$

The summation is defined in a certain domain around the regarded point. The equation can be modified by applying a Gaussian window for the integration. With an additional Gaussian derivative for the gradient computation Equation 2.4 is obtained. Since the voxels have only one grey-scale value computing a gradient of discrete values is not straight forward. It needs to be approximated. Due to noise in the image data it is beneficial to apply filter as noise is enhanced in differentiation. Smoothing (Gaussian filter) and gradient computation (Central difference scheme) are combined to a Gaussian derivative which is computationally more efficient. The so-called noise scale parameter σ indicates a domain size that is filtered for the gradient computation ∇V_σ. While the so-called integration scale parameter ρ characterises the standard deviation of the Gaussian kernel K_ρ. In other words, ρ defines the dimension in which the material orientation is analysed.

$$S = K_\rho (\nabla V_\sigma (\nabla V_\sigma)^T) \tag{2.4}$$

An eigendecomposition of S delivers the predominant material orientations. With its properties as symmetric and positive semi-definite tensor, three orthogonal eigenvectors accompanied by three positive eigenvalues are obtained. The smallest eigenvalue with its corresponding eigenvector indicates the fibre direction. In Figure 2.6 the structure tensor method is simplified shown for one pixel in a two dimensional case.

This approach does not require a perfect fibre resolution which allows for an enlarged field of view for the scanning. Furthermore, only two parameters (σ and ρ) must be defined and with distribution to multiple cores the calculations are scalable as well.

Karamov et al. [71] investigated the performance of different fibre orientation analyses. They compared the *XFiber* package from Avizo™, an *Ellipsometry* code and a *Structure Tensor* code. As evaluation procedure the methods were applied on 3D image data of a sample with continuous glass fibre (diameter 17 μm). The scans were performed with resolutions of $1.4, 3.2, 8$ and $16\,\mu$m. All methods generated accurate results. However, *XFiber* and *Ellipsometry* required the two highest resolutions, while the *Structure Tensor* code could produce accurate results for all resolutions. In addition, the *XFiber* package was regarded as computationally heavy.

Another approach for fibre orientation definition from Kagias et al. [72] uses a different imaging technology. They apply diffractive small angle X-ray scattering to extract the material orientation of injection moulded short fibre composites.

Similarly, the study from Kim et al. [73] moves away from image analysis towards a pure material orientation analysis. Their method is based on X-ray scattering tensor tomography, which is superior in terms of speed and field of view compared to classical image based X-ray computer tomography. In their study the orientation of continuous carbon fibres inserted into a $4 \times 4 \times 4\ mm^3$ polymethyl methacrylate matrix block could be obtained after approximately half an hour.

Several studies published in the last years deal with fibre bundle segmentation which can serve as bases for a boundary representation for finite element modelling. Investigations by Huang et al. [74], [75], [76] resulted in a segmentation approach for woven fabrics. It allows an individual fibre bundle segmentation by a manual approach. The accuracy depends on the number of slices along the bundles and the skills of the operator.

On the contrary to this manual approach Auenhammer et al. [77] presented three automated segmentation approaches. These differ in their degree of the boundary representation complexity. However, a more accurate representation results in a more complex segmentation algorithm. In the end the simplest approach was chosen and combined with a fibre tracking approach to reflect the local material orientation.

2.4 Image based finite element modelling

Generally two ways are followed to generate finite element meshes from tomography image data [78]. These are the voxel-based and the physical surface approaches. With the voxel method every image voxel is represented by a hexahedral finite element. Such a procedure can often be automated and is easier to realise, but can quickly lead to a large amount of elements. Furthermore, the boundary surface geometry is rather inaccurate which makes it difficult to compute stresses in this region. A study using a voxel-based method overcame this downside by applying a Gaussian smoothing operator [79]. This can be a valid approach, it comes however with a risk for penetrations of neighbouring fibre bundles. In their study they used the centre line of the fibre bundles as the material orientation. Straumit et al. [66] on the other hand used the above described structure tensor method to assign the local material orientation for their voxel-based model. In contrast to voxel-based models there are algorithms that create surface geometries during segmentation that can be meshed. For composites comprising of fibre bundles it is a common way to extract single slices through the volume and manually segment the fibre

bundles and interpolate the single cross-sections to a 3D body. Jespersen et al. [80] used Avizo™ and Geomagic Wrap® for this process. The study of Ewert et al. [81] used the freeware ImageJ for this process and compared the results with a voxel-based mesh. Both methods show similar tensile stiffness results after the created centre line for the fibre bundles was smoothed. It was concluded that a rough surface can lead to nonphysical material orientations.

A study recently presented by Sencu et al. [82] pursues a new idea for imaged based modelling by using a multi-scale approach. Their methodology describes a fibre centre line extraction, followed by a generation of eight small micro-scale models at a size of $50 \times 50 \times 50\ \mu m^3$. Those models characterise representative volume elements (RVEs) that are used to model the behaviour on the bundle scale. This avoids the described bundle centre lines or a material orientation mapping. However, it has to be noted, that local fibre misalignments might not be implemented in the model. Yet, the major advantage of this model can be rather found in the increased modelling opportunities. With this full multi-scale model the modelling is not restricted to the meso-scale but can account for effects on the fibre level.

3 Proposed procedure with examples

Our proposed X-ray computer tomography aided engineering (XAE) process (Figure 3.1) consists of a core process with *Image acquisition*, *Automated segmentation*, *Meshing* and *Mapping* which is unique for image based analysis. The process is not limited to non-crimp fabric reinforced polymers. It can be applied to other fibre reinforced composites with different architectures as well, e.g. woven fabrics or short fibre injection moulded parts. But also other materials like metal composites or bone structures have been successfully tested with this approach (not published yet). The main idea behind the proposed procedure is to create a boundary between fibre bundles and resin-rich areas and combine this with a fibre orientation analysis.

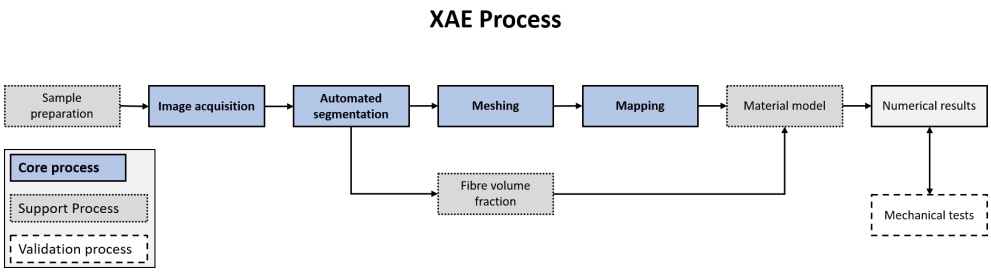

Figure 3.1: *XAE - X-ray computer tomography aided engineering process [77] with the core elements image acquisition, automated segmentation, meshing and mapping as well as the support process with sample preparation, fibre volume fraction determination and material model definition. The numerical results are validated with mechanical tests.*

Even though *Image acquisition* is part of the core process it has not been the key focus of this research project. However, it must be mentioned that the scanning and reconstruction processes are essential and all work-steps are built on the image acquisition. Consequently, high attention should be paid in order to align scanning settings and reconstruction methods with the end goal for the numerical modelling.

3.1 Automated segmentation

A core idea of XAE is to divide the segmentation in a surface segmentation and a fibre orientation analysis. The segmentation methods developed for *Paper B* aims to provide an automated, fast and accurate method, flexible enough to be adapted to other material types. It can be seen as major improvement to the presented methods in *Paper A*. For the surface segmentation in *Paper B* a thresholding (see Figure 2.4) and single fibre bundle segmentation (Figure 3.2) are used to extract the boundary between fibre bundles and resin-rich areas. The fibre orientation analysis is performed with the structure tensor approach for image analysis described above. Even though the thresholding was done with Avizo™, any other commercial segmentation software or freeware can be used since it is one of the standard segmentation methods. The second boundary segmentation is a

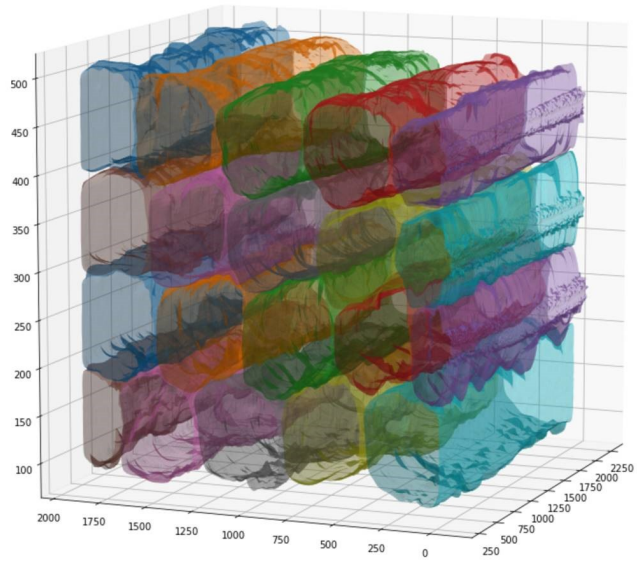

Figure 3.2: *Single fibre bundle segmentation created from unfolded volumes based on radially sampling the image intensities along each centre line. A penetration check prevents the volumes from intersecting each other.*

single bundle detection described in *Paper B*. It is programmed in a Python script where the image intensities are radially sampled along a centre line. The segmentation task is then regarded as a binary optimisation following Li et al. [83], extended by a penetration check [84].

For the orientation analysis in *Paper A* a fibre tracing method in Avizo™ was used (see Figure 2.5). This is expensive in terms of the required hardware, software and the computation time. The structure tensor code for *Paper B* (Figure 3.3) can be executed on a standard computer with a CPU of 32 GB RAM instead of an expensive machine designed for image analysis. Still the computation time is reduced by approximately 90 %. Additionally, the orientation analysis can be combined with the orientation mapping onto the finite element mesh in one Python script which further increases the user-friendliness. The advantages compared to *Paper A* can be summarised as:

a) Reduced software cost

b) Reduced hardware cost

c) Faster computation

d) Increased automation

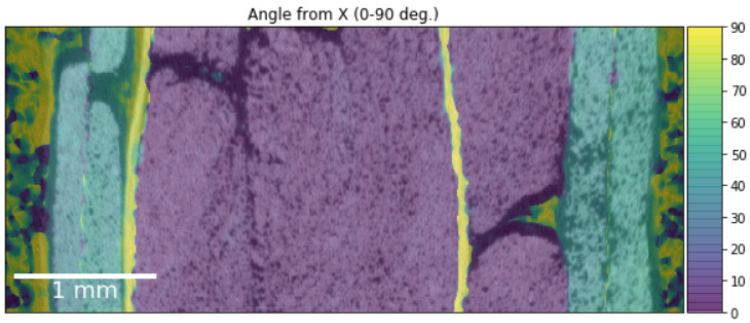

Figure 3.3: *Colour mapped voxels in a x-y plane of a non-crimp fabric reinforced composite representing the main fibre orientation per voxel. In purple areas the fibres are mainly oriented in the* 0° *direction, turquoise areas represent* ±45° *bi-axial layers and the yellow strips visualise the backing bundles orientated at* ±80°*. Since resin-rich areas do not have a dominant material orientation, the colours meander between yellow and blue. The Python script for the analysis is available at [85].*

3.2 Meshing

The mesh connects several different length scales. Meshing every single fibre is not possible with ten thousands of fibres in the scanned image. Thus, instead of single meshed fibres an element-wise fibre orientation mapping approach is chosen where one element represents several dozens of fibres. The larger the element size is selected the more challenging it becomes to account for small misalignment areas. Consequently, the mesh size and the parameters for the scanning, and even more for the orientation analysis with the structure tensor method must be concerted. The resolution must fulfil the requirements of the fibre orientation analysis to assure an accurate material orientation. Scans with a higher resolution than necessary, hence signify extra cost for scanning and image processing. Resolving every single fibre with a high resolution scan becomes therefore worthless if an average element size of 120 μm in *Paper A* or 200 μm in *Paper B* is chosen. With the structure tensor method the domain size ρ that is taken to estimate the material orientation in one voxel should be adjusted accordingly to the mesh size. Also the fibre diameter needs to be taken into consideration. This illustrates the need for a holistic view on XAE. One work step cannot be done without considering the effect on the following ones.

The high resolution scans that are usually necessary to run a fibre orientation analysis introduce a high level of detail on the boundary surface between fibre bundles and resin-rich areas. If a model on a several millimetre scale is of interest, this creates the need for a smoothed surface. Otherwise it would lead to an element number above 100 million elements. Consequently, the details in the surface need to be removed to keep the number of elements justifiable. If thresholding as segmentation method is used an experienced operator can create a complete solid mesh of the fibre bundles and the resin-rich areas with approximately 2.9 million elements in approximately 2 h, using a commercial pre-processor

like Ansa™.

The other option is to base the mesh on the single bundle segmentation method. The surface meshing of the fibre bundles is done in a Python script in a few seconds. The choice of the mesh type is decisive for the meshing effort. A mesh with tetrahedral elements can be created in a few minutes. On the other hand, due to the shape of the unidirectional bundles it can take several hours to create a hexahedral mesh with a commercial pre-processor.

3.3 Mapping

When the mesh of the fibre bundles is created, it can be used for the mapping algorithm. It is advantageous to spilt the segmentation work-step in a boundary segmentation and run the fibre orientation analysis later, after the meshing, together with the mapping algorithm. Two different methods are available. One is an element-wise, while the other one is an integration point-wise mapping approach.

The element-wise method is faster. The mesh input file can be directly loaded in the Python script and the fibre orientation is attached to the file in an executable Abaqus™ code. All types of elements are possible, shells and solids with different numbers of nodes and integration points. The code computes the centre of gravity for each element and extracts the fibre orientation of the voxel this calculated centre of gravity lies in. The result of the mapping can be viewed in a pre-processor like Ansa™ (Figure 3.4). The mapping with the Python code can take up to a few minutes, depending on the number of elements.

The integration point-wise mapping on the other hand is more complex due to the required Abaqus™ subroutine modelling. Furthermore, the coordinates of the integration points must be extracted before mapping. Therefore, a dummy simulation run is necessary, that outputs the coordinates of the integration points in an Abaqus™ .dat-file. This file is then loaded into the Python mapping code. For this method no centres of gravity need to be calculated. The coordinates of the integration points can be directly taken to obtain the fibre orientation for the domain around the integration point. Next, the material orientation is written in a Fortran 77 file. This file is later accessed via the Abaqus™ subroutine *ORIENT*. The compilation of this subroutine takes a substantial time, longer than simulating the actual load step in case of a simple tensile test. This method allows for a higher accuracy due to more evaluation points for higher order formulations per element, but it increases the simulation time at the same time.

3.4 Material modelling

The material behaviour was represented with a linear elastic orthotropic model. The six stiffness values and three Poisson´s ratios are obtained with the periodic boundary model EasyPBC [86]. For this model the fibre and matrix stiffness as well as the Poisson´s ratios are necessary. The fibre volume fraction is defined via the artificial fibre radius for this micro-mechanical model. The fibre volume fraction inside fibre bundles can be calculated

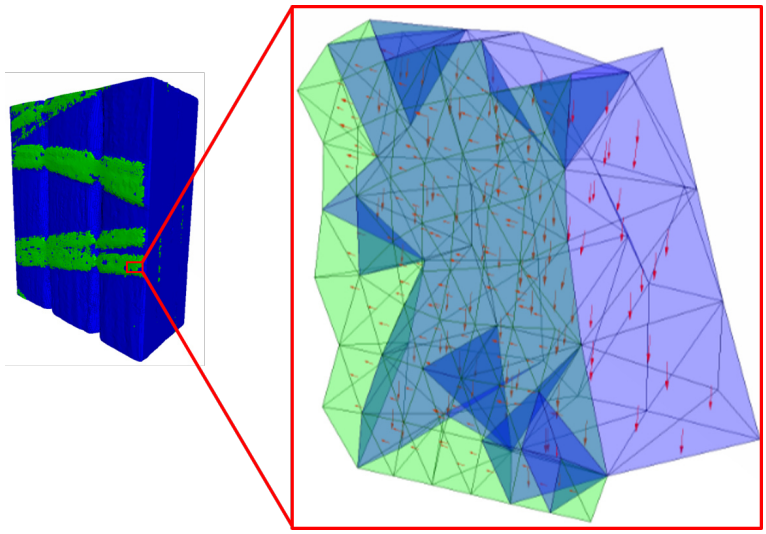

Figure 3.4: *Mapped material orientation for each single element based on a fibre orientation analysis [77] for a small part of the model displayed in the finite element pre-processor ANSA™. Red arrows indicate the main fibre orientation per element. Elements in blue belong to unidirectional with oriented in the* 0° *direction and elements in green belong to backing bundles with approximately* ±80°.

with data sheet values and the segmented volume of the fibre bundles.

$$V_{fbundle} = \frac{W_{FAW}\ n}{\rho_{fibres}} \frac{A_{surf}}{\chi_{bundle}} \tag{3.1}$$

Equation 3.1 describes this relationship where W_{FAW} stands for the fibre areal weight in the normalised $1m \times 1m$ area from the data sheet, n defines the number of bundle layers over the thickness, ρ_{fibres} represents the fibre´s density, χ_{bundle} is the volume of all unidirectional bundles and A_{surf} the area of the scanned surface parallel to the main fibre direction.

4 Results

The key achievement of this research project is the establishment of the X-ray computer tomography aided engineering process equipped with suitable tools for analysing the stress state in fibre composites for different load cases after manufacture. In this chapter a compilation of some of the capabilities of the XAE process is briefly summarised. It has to be mentioned that the capabilities are manifold and neither limited to the following examples nor to the considered material.

4.1 Stiffness

Table 4.1: Results from *Paper A* on the tensile modulus comparing the physical tests and the finite element model normalised with the H+ glass fibre modulus of three non-crimp reinforced composite samples.

	Sample-A	Sample-E	Sample-G
Physical test	0.51	0.54	0.52
XAE result	0.51	0.51	0.50
Difference	0.3 %	−4.8 %	−3.2 %

Newly introduced models are often developed to analyse complex material behaviour. In the current study, the XAE process is applied on unidirectional composites to model their response to longitudinal tension load, considering image data and data sheet values. Even Classical Laminate Theory would give a meaningful estimation of the elastic modulus, since the fibres in the investigated samples are mainly oriented in the same direction. The choice of problem for this study is motivated by the need to validate the XAE model concept. The goal for *Paper A* was therefore to assure the model capability to match the simplest case before moving on to more complex load cases. In Table 4.1 the elastic modulus results of the simulation model and the experimental tensile tests are compared. Details to the composite architecture, manufacture and tensile testing can be found in [77].

The stiffness results of the XAE process were assessed to be accurate given the slight underestimation of 2.8 % on average. The difference between the single test specimens, even though cut from the same part, differs more than the average deviation of the XAE result. The simulation results however fail to predict a correct trend.

4.2 Stress distribution

The true strength of XAE is that it enables a detailed stress state investigation after manufacture that accounts for flaws. For *Paper B* the main focus was not laid on the

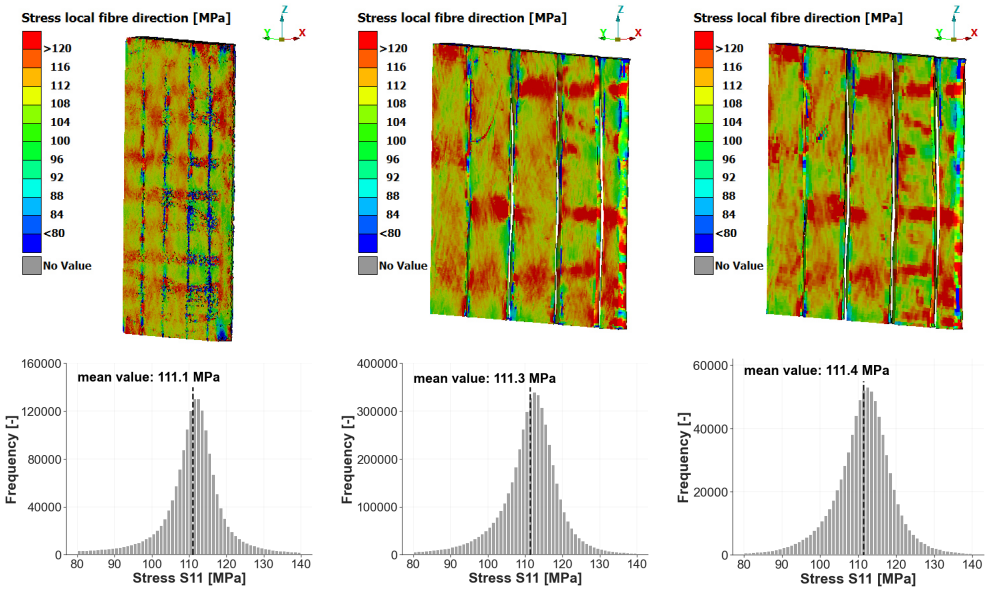

(a) *Tetrahedral mesh average element length* 200 μm

(b) *Hexahedral mesh average element length* 100 μm

(c) *Hexahedral mesh average element length* 200 μm

Figure 4.1: *Comparison of the influence of the average element length and the element type on the stress distribution in a y-z plane cross-section at the interface between backing bundles and unidirectional bundles (top row) and the stress distribution in the unidirectional bundles depicted with in histograms (bottom row). For the analysis hexahedral elements with a first order element formulation and tetrahedral elements with second order formulation have been used.*

stiffness results but developing the analysis for the stress distribution inside a non-crimp fabric composite shown for different parameters.

4.2.1 Mesh type and size

In tension-tension fatigue tests by Jespersen et al. [16] with a similar non-crimp reinforced glass fibre composite the backing bundles were detected as the cause for initial fibre breakage inside the unidirectional fibre bundles already at the first cycles. Thus, the cause must be a local stress concentration in the boundary layers of the unidirectional fibre bundles. In Figure 4.1 (top row) a plane cut close to backing bundles along the main fibre direction with the stresses in the element fibre orientation is visualised (in [87] an animation for the entire structure can be found). In this figure the experimentally postulated hypothesis can be supported, since stress concentrations can be clearly identified. With histograms (Figure 4.1 bottom row) the stress distribution can be quantified. In this study a model based on the thresholding segmentation method with second order

tetrahedral elements with an average element length of 200 μm is compared with two models based on the single bundle segmentation method with first order hexahedral elements and an average element length of 100 μm and 200 μm, respectively. Despite the variation in mesh type and size no major differences in the mean value of the stress distribution inside the unidirectional bundles occurs.

Moreover, the origin of the stress concentration is studied in this investigation. While the model in Figure 4.1 (a) includes backing bundles, they are missing in the models in Figure 4.1 (b) and (c). The stress concentrations are still occurring and are located in the same area. This leads to the conclusions that the fibre bundle waviness is the main reason for the stress concentrations. The fibre bundle waviness is initially introduced by the backing bundles and therefore the stress concentrations occur in the same area for the model with and without backing bundles, as further discussed in [62].

4.2.2 Mapping scheme

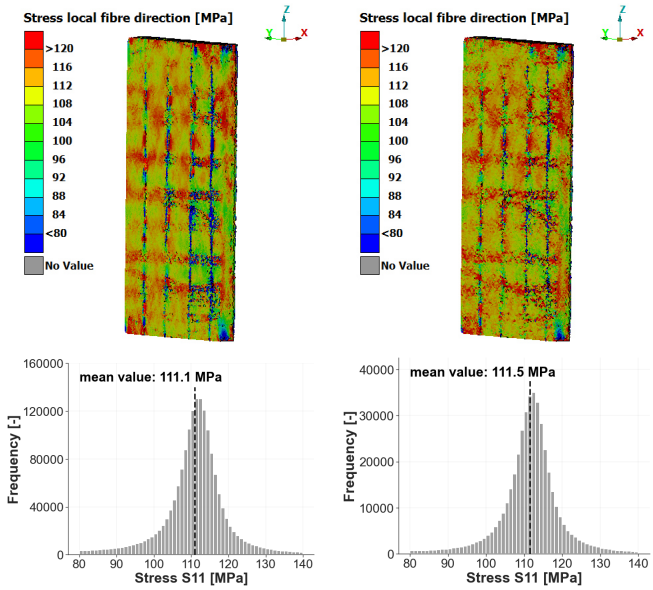

(a) *Integration point-wise mapping scheme*

(b) *Element-wise mapping scheme*

Figure 4.2: *Comparison of the influence of the mapping scheme on the outcome of the stress distribution in a y-z plane cross-section at the interface between backing bundles and unidirectional bundles (top row) and the stress distribution in the unidirectional bundles depicted in histograms (bottom row). The element-wise mapping simulation was run with first order elements, while the integration point-wise simulation was run with second order elements.*

For this study the two developed mapping schemes for *Paper B* are compared. One scheme offers a mapping of the material orientation for every integration point while the other offers only one orientation per element. The latter has a much shorter computation time. This advantage is further increased by using only first order elements compared to the second order elements for the integration point-wise mapping scheme run. In the end the run time was reduced by approximately 90 %.

Despite a smoother appearance of the stress distribution in Figure 4.2 (top row) no significant differences are visible. This impression is supported by the stress histograms (Figure 4.2 bottom row).

4.2.3 Resolution

In order to investigate limitations in the of the structure tensor image analysis combined with the developed orientation mapping algorithm, the image data was down-scaled. Therefore, an artificial binning of 2, 4 and 8 was applied. This means in each spatial direction 2, 4 and 8 voxels, respectively, were combined which reduces the data size by the factor 8, 64 and 512, respectively. For example, a binning of 8 corresponds to a resolution of 64 μm and a removal of 99.8 % of the original information of the scanned image. For the investigated glass fibre diameter of 17 μm it is not even possible for the human eye to detect single fibres for resolutions of 32 μm and 64 μm. The significant reduction in the data size comes with the advantage of a much faster computation of the structure tensor analysis. In Table 4.2 the influence on the mean stress in local fibre direction is listed as measure of the down-scaling effect.

Table 4.2: Effect of artificial down-scaling of the original X-ray computer tomography image scanned with 8 μm on the file size, the computation time of the structure tensor orientation code run on a computer with a CPU of 32 GB and the final result for the mean stress inside the unidirectional bundles in local fibre direction σ_{11}.

	8 μm	16 μm	32 μm	64 μm
File size $[MB]$	9459	1182	148	18
Information removed	–	87.5 %	98.4 %	99.8 %
Computation orientation analysis	20 min	4 min	2 min	30 s
Mean local σ_{11} $[MPa]$	111	110	106	101

In Figure 4.3 the effect can be studied closer. In the upper row additionally to the stress plots a visualisation of the actual image data, that was used for the analysis, is shown. Despite the highly smeared pixels for the 64 μm case, the stress concentrations inside the unidirectional bundles remain visible even for this low resolution analysis. However, they are less distinct, and the main colour goes more towards green. This observation is supported by the stress histograms in the bottom row of Figure 4.3. The mean stress is reduced by 9.09 % from 111 MPa to 101 MPa which causes the shift towards greener colours. Further, the areas with red colours in the stress plot above 120 MPa are

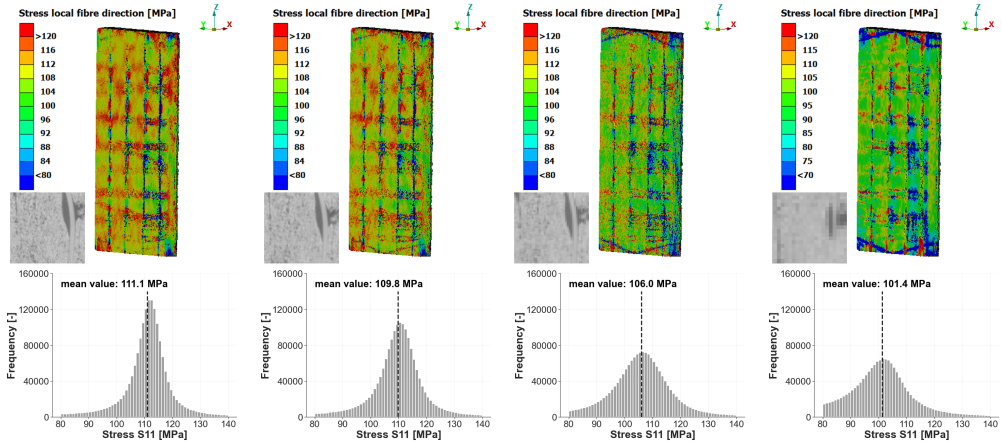

(a) 8 μm (b) 16 μm (c) 32 μm (d) 64 μm

Figure 4.3: *Visualisation of the influence of the computer tomography image resolution down-scaling on the outcome of the stress distribution in a y-z cross-section at the interface between backing bundles and unidirectional bundles (top row) and the stress distribution in the unidirectional bundles depicted with a histogram (bottom row). Examples for the image data quality are shown beside the stress plots in the top row.*

reduced due to this shift. In addition, the histogram distribution becomes flatter. Larger voxels lead to a smearing of distinct orientations. Especially finite elements in boundary regions of the unidirectional bundles will obtain an off-axis orientation from the off-axis bundles. Despite the less accurate stress distribution for the 64 μm case, it has to be kept in mind that the backing bundles only have a thickness of approximately 100 μm and an average mesh size of 200 μm was chosen. The structure tensor analysis together with the mapping algorithm is still capable of reflecting the low stresses that occur in the backing bundles.

The goal of this study was to identify and push the limits of XAE rather than to aim for the most accurate solution. It has to be emphasised that the down-scaling was carried out as post-processing. For a real scan and an especially designed reconstruction algorithm the results for the low-resolution results could be even improved. Theoretically, instead of the scanned length of approximately 30 mm of the original image with a resolution of 8 μm, a length of 240 mm would be possible for the resolution of 64 μm. This shifts the limits by almost two orders of magnitude. Those results demonstrate the large possibilities for future applications for XAE.

5 Concluding remarks

This research has led the groundwork for numerical modelling based on X-ray computer tomography. The proposed XAE procedure clearly focuses on two main important aspects, boundary representation and fibre orientation. It allows for great flexibility and can be expanded to other materials with a distinct material orientation as well. The method is fast, accurate, computationally cheap and automated. As biggest challenge for the user remains the meshing part.

Especially the combination with the structure tensor approach for the image analysis will shift the limits of the maximum field of view for scanning. Full wind turbine blades cannot be scanned and analysed, but for sub-parts in the range up to 0.5 m, it is now possible to achieve a detailed analysis of the stresses inside a structure after manufacture. The limiting factor has now shifted from the imaging part, here in particular the parameters field of view, resolution and data size, to the modelling part. In *Paper B* a finite element model with approximately 2.9 million elements has been used to show the stress distribution inside the non-crimp fabric reinforced polymer. The applied image analysis would yet allow for a field of view 64 times that of the scanned sample. This would consequently lead to a model with 180 million elements, which is not realistic.

Therefore, the advances in image analysis require new approaches for the modelling part. At the same time, a vast new playground has been opened. New multi-scale approaches can be applied, new load cases can be studied, the possibilities are manifold.

Now is the time to take advantage of the progress in imaging and segmentation.

6 Summary of appended papers

Summary Paper A

In *Paper A* for the first time a full procedure for creating finite element models based on X-ray computer tomography including an automated segmentation method for non-crimp fabrics is proposed. Further, this procedure offers an element-wise fibre orientation mapping.

Summary Paper B

In *Paper B* an improved procedure for finite element analysis based on X-ray computer tomography is presented. The new methodology reduces the time and the software cost by increasing at the same time the accuracy and the degree of automation.

References

[1] *IEA (2019), Offshore Wind Outlook 2019, IEA, Paris.* https://www.iea.org/reports/offshore-wind-outlook-2019. Accessed: 2020-08-18.

[2] *United Nations Resolution adopted by the General Assembly on 25 September 2015. 70/1. Transforming our world: the 2030 Agenda for Sustainable Development.* https://www.un.org/ga/search/view_doc.asp?symbol=A/RES/70/1&Lang=E. Accessed: 2020-12-26.

[3] *Proposal for a Regulation of the European Parliament and the Council establishing the framework for achieving climate neutrality and amending Regulation (EU) 2018/1999 (European Climate Law).* https://eur-lex.europa.eu/legal-content/EN/TXT/?qid=1596443911913&uri=CELEX:52019DC0640#document2. Accessed: 2020-08-18.

[4] W. Ostachowicz et al. *MARE-WINT: New materials and reliability in offshore wind turbine technology.* Springer Open, 2016. DOI: 10.1007/978-3-319-39095-6.

[5] G. M. Moisé. Corruption in the oil sector: A systematic review and critique of the literature. *Extractive Industries and Society* **7** (2020), 217–236. DOI: 10.1016/j.exis.2020.01.002.

[6] *IEA, Offshore wind technical potential and electricity demand in selected countries, 2018, IEA, Paris.* https://www.iea.org/data-and-statistics/charts/offshore-wind-technical-potential-and-electricity-demand-in-selected-countries-2018. Accessed: 2020-08-18.

[7] *Global Wind Energy Council - Wind Power a cornerstone of the Global Economic Recovery.* https://gwec.net/wp-content/uploads/2020/06/Green-Recovery-Statement-EN-2.pdf. Accessed: 2020-08-18.

[8] L. P. Mikkelsen. *The fatigue damage evolution in the load-carrying composite laminates of wind turbine blades. In Fatigue Life Prediction of Composites and Composite Structures.* 2nd ed. Elsevier Ltd., Duxford, United Kingdom, 2020, pp. 569–603. DOI: 10.1016/b978-0-08-102575-8.00016-4.

[9] G. A. Bibo, P. J. Hogg, and M. Kemp. Mechanical characterisation of glass- and carbon-fibre-reinforced composites made with non-crimp fabrics. *Composites Science and Technology* **57** (1997), 1221–1241. DOI: 10.1016/s0266-3538(97)00053-5.

[10] P. J. Liotier, V. Alain, and D. Christine. Characterization of 3D morphology and microcracks in composites reinforced by multi-axial multi-ply stitched preforms. *Composites Part A: Applied Science and Manufacturing* **41** (2010), 653–662. DOI: 10.1016/j.compositesa.2010.01.015.

[11] M. Saeedifar et al. Damage assessment of NCF, 2D and 3D woven composites under compression after multiple-impact using acoustic emission. *Composites Part A: Applied Science and Manufacturing* **132** (2020), 105833. DOI: 10.1016/j.compositesa.2020.105833.

[12] A. Shipsha and M. Burman. Failure mechanisms in NCF composite bolted joints: Experiments and FE model. *Composites Part B: Engineering* **192** (2020), 107950. DOI: 10.1016/j.compositesb.2020.107950.

[13] A. S. Argon. *Fracture of composites*. Vol. 1. ACADEMIC PRESS, INC., 1988, pp. 79–113. DOI: 10.1016/b978-0-12-341801-2.50007-2.

[14] D. Wilhelmsson et al. Compressive strength assessment of fibre composites based on a defect severity model. *Composites Science and Technology* **181** (2019), 107685. DOI: 10.1016/j.compscitech.2019.107685.

[15] J. Zangenberg, P. Brøndsted, and J. W. Gillespie. Fatigue damage propagation in unidirectional glass fibre reinforced composites made of a non-crimp fabric. *Journal of Composite Materials* **48** (2014), 2711–2727. DOI: 10.1177/0021998313502062.

[16] K. M. Jespersen et al. Uncovering the fatigue damage initiation and progression in uni-directional non-crimp fabric reinforced polyester composite. *Composites Part A: Applied Science and Manufacturing* **109** (2018), 481–497. DOI: 10.1016/j.compositesa.2018.03.002.

[17] H. Heß, Y. C. Roth, and N. Himmel. Elastic constants estimation of stitched NCF CFRP laminates based on a finite element unit-cell model. *Composites Science and Technology* **67** (2007), 1081–1095. DOI: 10.1016/j.compscitech.2006.05.024.

[18] V. Yavari and M. H. Kadivar. Application of stochastic finite element method in estimation of elastic constants for NCF composites. *Mechanics Research Communications* **40** (2012), 69–76. DOI: 10.1016/j.mechrescom.2012.01.013.

[19] D. Wilhelmsson et al. An experimental study of fibre waviness and its effects on compressive properties of unidirectional NCF composites. *Composites Part A: Applied Science and Manufacturing* **107** (2018), 665–674. DOI: 10.1016/j.compositesa.2018.02.013.

[20] A. Shipsha, S. Hallström, and M. Burman. Effect of stacking sequence and bundle waviness in quasi-isotropic NCF composites subjected to compression. *Composites Part B: Engineering* **178** (2019), 107423. DOI: 10.1016/j.compositesb.2019.107423.

[21] F. Edgren et al. Formation of damage and its effects on non-crimp fabric reinforced composites loaded in tension. *Composites Science and Technology* **64** (2004), 675–692. DOI: 10.1016/S0266-3538(03)00292-6.

[22] A. Shipsha, M. Burman, and J. Ekh. Failure of cross-ply NCF composites under off-axis compressive loads - An experimental study and a new strength prediction model including fibre bundle waviness. *Composites Part B: Engineering* **153** (2018), 49–56. DOI: 10.1016/j.compositesb.2018.06.022.

[23] R. Joffe et al. Compressive failure analysis of non-crimp fabric composites with large out-of-plane misalignment of fiber bundles. *Composites Part A: Applied Science and Manufacturing* **36** (2005), 1030–1046. DOI: 10.1016/j.compositesa.2004.10.028.

[24] F. Edgren, L. E. Asp, and R. Joffe. Failure of NCF composites subjected to combined compression and shear loading. *Composites Science and Technology* **66** (2006), 2865–2877. DOI: 10.1016/j.compscitech.2006.02.021.

[25] E. Marklund, L. E. Asp, and R. Olsson. Transverse strength of unidirectional non-crimp fabric composites: Multiscale modelling. *Composites Part B: Engineering* **65** (2014), 47–56. DOI: 10.1016/j.compositesb.2014.01.053.

[26] S. Nonn, C. Kralovec, and M. Schagerl. Damage mechanisms under static and fatigue loading at locally compacted regions in a high pressure resin transfer molded carbon

fiber non-crimp fabric. *Composites Part A: Applied Science and Manufacturing* **115** (2018), 57–65. DOI: 10.1016/j.compositesa.2018.09.011.

[27] L. M. Ferreira, E. Graciani, and F. París. Predicting failure load of a non-crimp fabric composite by means of a 3D finite element model including progressive damage. *Composite Structures* **225** (2019), 111115. DOI: 10.1016/j.compstruct.2019.111115.

[28] S. Costa, M. Fagerström, and R. Olsson. Development and validation of a finite deformation fibre kinking model for crushing of composites. *Composites Science and Technology* **197** (2020), 108236. DOI: 10.1016/j.compscitech.2020.108236.

[29] H. Villarraga-Gómez, E. L. Herazo, and S. T. Smith. X-ray computed tomography: from medical imaging to dimensional metrology. *Precision Engineering* **60** (2019), 544–569. DOI: 10.1016/j.precisioneng.2019.06.007.

[30] R. Chang and J. W. J. Thoman. *Physical Chemistry for the Chemical Sciences*. University Science Books, Canada, 2015.

[31] R. Clack. Towards a complete description of three-dimensional filtered backprojection. *Physics in Medicine and Biology* **37** (1992), 645–660. DOI: 10.1088/0031-9155/37/3/011.

[32] K. J. Batenburg and L. Plantagie. Fast approximation of algebraic reconstruction methods for tomography. *IEEE Transactions on Image Processing* **21** (2012), 3648–3658. DOI: 10.1109/TIP.2012.2197012.

[33] S. Magkos, A. Kupsch, and G. Bruno. Direct Iterative Reconstruction of Computed Tomography Trajectories Reconstruction from limited number of projections with DIRECTT. *Review of Scientific Instruments* **91** (2020), 103107. DOI: 10.1063/5.0013111.

[34] R. Cierniak. *X-Ray Computed Tomographyin Biomedical Engineering*. Springer-Verlag London Limited, 2011.

[35] C. Shi et al. Wide activation for accurate and fast computed tomography reconstruction in limited-angle problem. *Nuclear Instruments and Methods in Physics Research, Section A: Accelerators, Spectrometers, Detectors and Associated Equipment* **977** (2020), 164293. DOI: 10.1016/j.nima.2020.164293.

[36] F. Yang et al. Cupping artifacts correction for polychromatic X-ray cone-beam computed tomography based on projection compensation and hardening behavior. *Biomedical Signal Processing and Control* **57** (2020), 101823. DOI: 10.1016/j.bspc.2019.101823.

[37] R. Gordon, R. Bender, and G. T. Herman. Algebraic Reconstruction Techniques (ART) for three-dimensional electron microscopy and X-ray photography. *Journal of Theoretical Biology* **29** (1970), 471–476. DOI: https://doi.org/10.1016/0022-5193(70)90109-8.

[38] K. Lange and R. Carson. EM reconstruction algorithms for emission and transmission tomography. *Journal of Computer Assisted Tomography* **8** (1984), 306–316.

[39] M. Akagi et al. Deep learning reconstruction improves image quality of abdominal ultra-high-resolution CT. *European Radiology* **29** (2019), 6163–6171. DOI: 10.1007/s00330-019-06170-3.

[40] J. Fu, J. Dong, and F. Zhao. A Deep Learning Reconstruction Framework for Differential Phase-Contrast Computed Tomography with Incomplete Data. *IEEE*

Transactions on Image Processing **29** (2020), 2190–2202. DOI: 10.1109/TIP.2019.2947790. arXiv: 1904.00531.

[41] M. van Eijnatten et al. 3D deformable registration of longitudinal abdominopelvic CT images using unsupervised deep learning (2020). arXiv: 2005.07545.

[42] *The ASTRA Toolbox*. https://www.astra-toolbox.com/. Accessed: 2020-10-06.

[43] A. Wilbers et al. Application of iterative reconstruction algorithms to mitigate CT-artefacts when measuring fiber reinforced polymer materials. *Polymer* **177** (2019), 120–130. DOI: 10.1016/j.polymer.2019.06.004.

[44] H. Der Sarkissian et al. A cone-beam X-ray computed tomography data collection designed for machine learning. *Scientific data* **6** (2019), 215. DOI: 10.1038/s41597-019-0235-y. arXiv: 1905.04787.

[45] J. W. Buurlage et al. Real-time reconstruction and visualisation towards dynamic feedback control during time-resolved tomography experiments at TOMCAT. *Scientific Reports* **9** (2019), 18379. DOI: 10.1038/s41598-019-54647-4.

[46] E. Maire and P. J. Withers. Quantitative X-ray tomography. *International Materials Reviews* **59** (2014), 1–43. DOI: 10.1179/1743280413Y.0000000023.

[47] W. Ren et al. Two-dimensional X-ray CT image based meso-scale fracture modelling of concrete. *Engineering Fracture Mechanics* **133** (2015), 24–39. DOI: 10.1016/j.engfracmech.2014.10.016.

[48] M. Naeimi et al. Reconstruction of the rolling contact fatigue cracks in rails using X-ray computed tomography. *NDT and E International* **92** (2017), 199–212. DOI: 10.1016/j.ndteint.2017.09.004.

[49] M. A. Harimon et al. High temperature fatigue characteristics of P/M and hot-forged W-Re and TZM for X-ray target of CT scanner. *Materials and Design* **137** (2018), 335–344. DOI: 10.1016/j.matdes.2017.10.044.

[50] S. Garcea, Y. Wang, and P. Withers. X-ray computed tomography of polymer composites. *Composites Science and Technology* **156** (2018), 305–319. DOI: 10.1016/J.COMPSCITECH.2017.10.023.

[51] M. J. Emerson et al. Statistical validation of individual fibre segmentation from tomograms and microscopy. *Composites Science and Technology* **160** (2018), 208–215. DOI: 10.1016/j.compscitech.2018.03.027.

[52] D. Wilhelmsson et al. Influence of in-plane shear on kink-plane orientation in a unidirectional fibre composite. *Composites Part A: Applied Science and Manufacturing* **119** (2019), 283–290. DOI: 10.1016/j.compositesa.2019.01.018.

[53] Y. Wang et al. Evolution of kink bands in a notched unidirectional carbon fibre-epoxy composite under four-point bending. *Composites Science and Technology* **172** (2019), 143–452. DOI: 10.1016/j.compscitech.2019.01.014.

[54] M. J. Lagerwerf et al. Noise2Filter: Fast, self-supervised learning and real-time reconstruction for 3D computed tomography. *Machine Learning: Science and Technology* **2** (2021), 015012. DOI: 10.1088/2632-2153/abbd4d.

[55] F. Marone et al. Towards on-the-fly data post-processing for real-time tomographic imaging at TOMCAT. *Advanced Structural and Chemical Imaging* **3** (2017), 1. DOI: 10.1186/s40679-016-0035-9.

[56] *User's Guide Avizo Software 2019*. https://assets.thermofisher.com/TFS-Assets/MSD/Product-Guides/users-guide-avizo-software-2019.pdf. Accessed: 2020-02-25.

[57] B. J. Blinzler et al. "A Systematic Approach to Transforming Composite 3D Images Into Meso-Scale Computational Models". *18th European Conference on Composite Materials*. Athens, Greece, 2018.

[58] M. J. Emerson et al. Individual fibre segmentation from 3D X-ray computed tomography for characterising the fibre orientation in unidirectional composite materials. *Composites Part A: Applied Science and Manufacturing* **97** (2017), 83–92. DOI: 10.1016/j.compositesa.2016.12.028.

[59] C. Eberhardt et al. Fibre-orientation measurements in short-glass-fibre compsites - II: A quantitative error estimate of the 2D image analysis technique. *Composites Science and Technology* **61** (2001), 1961–1974. DOI: 10.1016/S0266-3538(01)00106-3.

[60] R. Blanc et al. Fiber orientation measurements in composite materials. *Composites Part A: Applied Science and Manufacturing* **37** (2006), 197–206. DOI: 10.1016/j.compositesa.2005.04.021.

[61] A. T. Zehnder, V. Patel, and T. J. Rose. Micro-CT Imaging of Fibers in Composite Laminates under High Strain Bending. *Experimental Techniques* **44** (2020), 531–540. DOI: 10.1007/s40799-020-00374-9.

[62] R. M. Auenhammer et al. X-ray tomography based numerical analysis of stress concentrations in non-crimp fabric reinforced composites - assessment of segmentation methods. *IOP Conference Series: Materials Science and Engineering* **942** (2020), 012038. DOI: 10.1088/1757-899X/942/1/012038.

[63] N. Q. Nguyen et al. Micro-CT measurement of fibre misalignment: Application to carbon/epoxy laminates manufactured in autoclave and by vacuum assisted resin transfer moulding. *Composites Part A: Applied Science and Manufacturing* **104** (2018), 14–23. DOI: 10.1016/j.compositesa.2017.10.018.

[64] S. G. Advani and C. L. Tucker. The Use of Tensors to Describe and Predict Fiber Orientation in Short Fiber Composites. *Journal of Rheology* **31** (1987), 751–784. DOI: 10.1122/1.549945.

[65] R. S. Bay and C. L. Tucker. Fiber orientation in simple injection moldings. Part I: Theory and numerical methods. *Polymer Composites* **13** (1992), 317–331. DOI: 10.1002/pc.750130409.

[66] I. Straumit, S. V. Lomov, and M. Wevers. Quantification of the internal structure and automatic generation of voxel models of textile composites from X-ray computed tomography data. *Composites Part A: Applied Science and Manufacturing* **69** (2015), 150–158. DOI: 10.1016/j.compositesa.2014.11.016.

[67] I. Straumit et al. Computation of permeability of a non-crimp carbon textile reinforcement based on X-ray computed tomography images. *Composites Part A: Applied Science and Manufacturing* **81** (2016), 289–295. DOI: 10.1016/j.compositesa.2015.11.025.

[68] C. Oddy et al. A framework for macroscale modelling of inelastic deformations in 3D-woven composites. *Mechanics of Materials* **(In Press)** (2021), 103856. DOI: 10.1016/j.mechmat.2021.103856.

[69] P. P. Camanho et al. Three-dimensional invariant-based failure criteria for fibre-reinforced composites. *International Journal of Solids and Structures* **55** (2015), 92–107. DOI: 10.1016/j.ijsolstr.2014.03.038.

[70] N. Jeppesen et al. Characterization of the fiber orientations in non-crimp glass fiber reinforced composites using structure tensor. *IOP Conference Series: Materials Science and Engineering* **942** (2020), 012037. DOI: 10.1088/1757-899x/942/1/012037.

[71] R. Karamov et al. Micro-CT based structure tensor analysis of fibre orientation in random fibre composites versus high-fidelity fibre identification methods. *Composite Structures* **235** (2020), 111818. DOI: 10.1016/j.compstruct.2019.111818.

[72] M. Kagias et al. Diffractive small angle X-ray scattering imaging for anisotropic structures. *Nature Communications* **10** (2019), 5130. DOI: 10.1038/s41467-019-12635-2.

[73] J. Kim et al. X-ray scattering tensor tomography with circular gratings. *Applied Physics Letters* **116** (2020), 134102. DOI: 10.1063/1.5145361.

[74] W. Huang et al. Reconstruction of mesostructural material twin models of engineering textiles based on Micro-CT Aided Geometric Modeling. *Composites Part A: Applied Science and Manufacturing* **124** (2019), 105. DOI: 10.1016/j.compositesa.2019.105481.

[75] W. Huang et al. Transverse compaction of 2D glass woven fabrics based on material twins – Part I: Geometric analysis. *Composite Structures* **237** (2020), 111929. DOI: 10.1016/j.compstruct.2020.111929.

[76] W. Huang et al. Transverse compaction of 2D glass woven fabrics based on material twins – Part II: Tow and fabric deformations. *Composite Structures* **237** (2020), 111963. DOI: 10.1016/j.compstruct.2020.111963.

[77] R. M. Auenhammer et al. Automated X-ray computer tomography segmentation method for finite element analysis of non-crimp fabric reinforced composites. *Composite Structures* **256** (2021), 113136. DOI: 10.1016/j.compstruct.2020.113136.

[78] R. M. Sencu et al. Generation of micro-scale finite element models from synchrotron X-ray CT images for multidirectional carbon fibre reinforced composites. *Composites Part A: Applied Science and Manufacturing* **91** (2016), 85–95. DOI: 10.1016/j.compositesa.2016.09.010.

[79] B. Wintiba et al. Automated reconstruction and conformal discretization of 3D woven composite CT scans with local fiber volume fraction control. *Composite Structures* **248** (2020), 112438. DOI: 10.1016/j.compstruct.2020.112438.

[80] K. M. Jespersen et al. "X-ray tomography based finite element modelling of non-crimp fabric based fibre composite". *18th European Conference on Composite Materials*. Athens, Greece, 2018.

[81] A. Ewert et al. Predicting the overall response of an orthogonal 3D woven composite using simulated and tomography-derived geometry. *Composite Structures* **243** (2020), 112169. DOI: 10.1016/j.compstruct.2020.112169.

[82] R. M. Sencu et al. Multiscale image-based modelling of damage and fracture in carbon fibre reinforced polymer composites. *Composites Science and Technology* **198** (2020), 108243. DOI: 10.1016/j.compscitech.2020.108243.

[83] Kang Li et al. Optimal Surface Segmentation in Volumetric Images-A Graph-Theoretic Approach. *IEEE Trans. Pattern Anal. Mach. Intell.* **28** (2006), 119–134. DOI: 10.1109/TPAMI.2006.19.

[84] N. Jeppesen et al. "Sparse Layered Graphs for Multi-Object Segmentation". *2020 IEEE/CVF Conf. Comput. Vis. Pattern Recognit.* IEEE, June 2020, pp. 12774–12782. DOI: 10.1109/CVPR42600.2020.01279.

[85] N. Jeppesen et al. Characterization of the Fiber Orientations in Non-Crimp Glass Fiber Reinforced Composites using Structure Tensor. *[Data set]. Zenodo.* (2020). DOI: http://doi.org/10.5281/zenodo.3877522.

[86] S. L. Omairey, P. D. Dunning, and S. Sriramula. Development of an ABAQUS plugin tool for periodic RVE homogenisation. *Engineering with Computers* **35** (2019), 567–577. DOI: 10.1007/s00366-018-0616-4.

[87] R. M. Auenhammer et al. Automated X-ray computer tomography segmentation method for finite element analysis of non-crimp fabric reinforced composites. *[Data set]. Zenodo.* (2020). DOI: http://doi.org/10.5281/zenodo.3830790.